Formation and decay of ^{164}Yb* in near- and below-barrier fusion reactions

N. G. Nicolis and D. G. Sarantites
Department of Chemistry, Washington University, St. Louis, Missouri 63130
(Received 9 July 1993)

A consistent description of the formation and decay of ^{164}Yb* in the fusion of ^{16}O + ^{148}Sm and ^{64}Ni + ^{100}Mo is presented in a bombarding energy range from near to well below the entrance channel Coulomb barrier. Fusion excitation functions and angular momentum distributions are described well with a recently proposed one-dimensional barrier penetration model with energy-dependent fusion barriers. The main features of fusion and angular momentum distribution data in ^{64}Ni + ^{100}Mo are also reproduced with simplified coupled channel calculations. The statistical model accounts well for the decay of ^{164}Yb* in the ^{16}O-induced reaction and for most of the data in the ^{64}Ni-induced reaction. The evaporation residue fractional cross sections as a function of the compound nucleus excitation energy show trends that correlate with the low- and high-spin regions of the compound nucleus angular momentum distributions populated in the two reactions.

PACS number(s): 25.70.Gh, 25.70.Jj, 24.60.Dr, 24.10.Eq

I. INTRODUCTION

The process of subbarrier fusion between medium to heavy-mass nuclei has attracted a great deal of interest in recent years. Numerous experimental observations have established that although the near-barrier fusion cross sections are described well by a one-dimensional barrier penetration model, the below-barrier cross sections may exceed these predictions by orders of magnitude [1]. Recent studies have employed measurements of evaporation residue γ multiplicities, fission fragment angular anisotropies, and isomer ratios in order to deduce the moments of the spin distributions of the fused systems. A broadening of the spin distributions has been observed in several systems that exhibit a subbarrier cross section enhancement [2]. Theoretical approaches developed in order to understand these effects include the coupled-channels method [3–6] as well as several models dealing with the fusion process from different points of view [7–15]. The coupled-channels method has demonstrated the importance of coupling of the entrance channel to various inelastic and transfer degrees of freedom in the subbarrier fusion enhancement. It also predicts the subbarrier fusion enhancement as well as the broadening of the spin distributions compared to the one-dimensional barrier penetration model.

It has been realized [2,16] that stringent tests of the fusion models can be made from comparisons with both fusion excitation functions and moments of the spin distributions, whenever available. A systematic analysis of cross section and average angular momentum data extracted with the aforementioned techniques was recently undertaken by DiGregorio and Stokstad [16]. The data were compared with a barrier penetration model including the effect of coupling to the low-lying inelastic channels. It was concluded that in most of the cases the simplified coupled-channels calculations that fit the cross sections also give a resonable account of the measured angular momenta. A few exceptions occur in systems involving highly fissile compound nuclei as well as the most symmetric systems such as ^{64}Ni + ^{100}Mo and ^{80}Se + ^{80}Se studied with the γ-multiplicity technique. In the latter systems, the theory was found to underestimate systematically the fusion cross section and the corresponding average angular momentum with decreasing bombarding energy.

The subbarrier fusion of ^{64}Ni + ^{100}Mo was studied first with the Oak Ridge Spin Spectrometer by Halbert *et al.* [17,18]. Evaporation residue cross sections and γ-ray multiplicity distributions were measured for the dominant decay channels. The compound nucleus spin distributions were reconstructed from the the γ-multiplicity distributions using statistical model estimates of the angular momentum removed by particle and γ-ray emission. Using the same model as DiGregorio and Stokstad, it was found that the excitation function cannot be reproduced with *a priori* coupling strengths. Increasing the coupling strengths to 1.5 times their expected values was found necessary to fit the cross sections. However, even with this modification the average angular momenta were still underestimated [17]. A reanalysis of the ^{64}Ni + ^{100}Mo data was recently reported in which the treatment of events originating from low compound nucleus spins was examined [18]. In the latter analysis, the ℓ dependence of the angular momentum removed by neutron and γ-ray emission in the conversion of the γ multiplicity to compound nucleus spin distributions was taken into account. That analysis showed a slight increase in the average angular momentum and a small decrease in the magnitude of the fusion cross sections. However, these corrections did not alter the previous discrepancies between the data and theoretical predictions [17]. The data set of Refs. [17,18] provides one of the most complete subbarrier fusion measurements available for a heavy and nearly symmetric entrance channel. Therefore, it is not surprising that the observed effects have initiated several theoretical investigations and comparative studies [2,9,12,16].

In principle, a coupled-channels approach should be able to account for the experimental data once the appropriate coupling scheme is known. However, this procedure becomes quite involved or even impractical when the number of contributing channels is large. It was shown recently by Mohanty *et al.* [8,9] that the results of a model coupled-channels calculation can be reproduced by a simple barrier penetration model with energy-dependent barriers. It was pointed out that the barrier heights should be expressed as a function of the radial kinetic energy at the barrier radius. Such an energy dependence is expected on the basis of a macroscopic model of shape evolutions describing fusion [14,15].

Below, we present a description of the reactions ^{64}Ni + ^{100}Mo and ^{16}O + ^{148}Sm through the model of Mohanty *et al.* Both reactions lead to the formation of the compound nucleus ^{164}Yb*. Evaporation residue cross section and spin distribution data [17–19] are considered together with recent data on these reactions [20]. The bombarding energies range from near to well below the respective entrance channel Coulomb barriers. A satisfactory understanding of the ^{64}Ni + ^{100}Mo reaction can be obtained with energy-dependent fusion barriers extracted from the experimental spin distributions. A good description of the fusion excitation function and the first two moments of the compound nucleus spin distributions is thus obtained. Furthermore, the calculated spin distributions are sufficient in reproducing, through the statistical model, the majority of the evaporation residue cross sections in both reactions. Using the asymmetric ^{16}O + ^{148}Sm reaction as a reference, it is realized that the nearly symmetric ^{64}Ni + ^{100}Mo system involves a much larger angular momentum transfer to the compound nucleus. This significantly influences the cross sections of the neutron evaporation channels. In particular, it leads to an enhancement of the fractional $2n$ and a suppression of the fractional $4n$ cross sections, for ^{64}Ni + ^{100}Mo, in the bombarding energy range of the present study. Comparisons of the data with simplified coupled-channels calculations are also made for ^{64}Ni + ^{100}Mo. Most of the features of the available data are reproduced by including coupling strengths additional to those of the low-lying projectile and the target inelastic excitation modes.

II. FUSION PROCESS

The fusion cross section $\sigma_f(E)$ and the moments of the spin distributions leading to fusion $\langle \ell^n \rangle$ are given by

$$\sigma_f(E) = \sum_{\ell=0}^{\infty} \sigma_\ell(E) \tag{1}$$

and

$$\langle \ell^n \rangle = \frac{\sum \ell^n \sigma_\ell(E)}{\sum \sigma_\ell(E)} \tag{2}$$

in terms of the partial wave cross section

$$\sigma_\ell = \pi \lambda^2 (2\ell + 1) T_\ell, \tag{3}$$

where E denotes the center of mass energy and λ is the reduced asymptotic wavelength of the relative motion.

In the one-dimensional barrier penetration model (BPM), the transmission coefficients T_ℓ are usually obtained in a parabolic approximation of the total (Coulomb + nuclear + centrifugal) potential at the maximum, which defines the *fusion radius* $R_{b\ell}$. This results in an angular-momentum-dependent *fusion barrier* $V_{b\ell}$ representing the total potential at $R_{b\ell}$ with a *curvature*

$$\hbar\omega_\ell = \left| \frac{\hbar^2}{2\mu} \frac{d^2 V_{b\ell}}{dr^2} \right|^{1/2}_{r=R_{b\ell}}. \tag{4}$$

The transmission coefficients, in this approximation, are given by

$$T_\ell = \left\{ 1 + \exp\left[\frac{2\pi}{\hbar\omega_\ell} (V_{b\ell} - E) \right] \right\}^{-1}. \tag{5}$$

In the Wong approximation [21] ($R_{b\ell} = R_{b0} \equiv R_b$, $\hbar\omega_\ell = \hbar\omega_0$), the fusion barrier is expressed as

$$V_{b\ell} = V_b + \frac{\ell(\ell+1)\hbar^2}{2\mu R_b^2} \tag{6}$$

and a closed form expression is obtained for the fusion cross section,

$$\sigma_f(E) = \frac{\hbar\omega R_b^2}{2E} \ln\left[1 + \exp\left\{ 1 + \exp \frac{2\pi}{\hbar\omega}(E - V_b) \right\} \right]. \tag{7}$$

The subbarrier fusion enhancement over the predictions of Eq. (7) is described in the energy-dependent barrier penetration model (EDBPM) of Mohanty *et al.* [8] by allowing V_b to become a function of the radial kinetic energy ϵ at the barrier radius:

$$V_b = V_b(\epsilon) \equiv V_b\left(E - \frac{\ell(\ell+1)\hbar^2}{2\mu R_b^2} \right). \tag{8}$$

The following parametrization of the fusion barrier was proposed:

$$V_b = \begin{cases} V_2 & \text{for } \epsilon \geq E_2, \\ V_1 + \frac{(V_2 - V_1)}{(E_2 - E_1)}(\epsilon - E_1) & \text{for } E_1 < \epsilon < E_2, \\ V_1 & \text{for } \epsilon \leq E_1, \end{cases} \tag{9}$$

where V_2 and V_1 are the so-called sudden and adiabatic barrier heights [9] occurring at ϵ=E_2 and E_1, respectively. The transition between these limits is made with the linear term in Eq. (9). The form of this parametrization has been suggested by a macroscopic model of nuclear shape evolutions applied in the description of subbarrier fusion reactions [14,15]. As shown in Ref. [8], the predicted fusion cross sections and angular momentum distributions by the EDBPM can be made equivalent to the more elaborate treatments of coupled-channels calculations. Systematic trends in V_1, V_2, E_1, E_2 extracted by the requirement to reproduce measured fusion excita-

tion functions in several systems were recently reported [9].

In the following calculations, we employ a Woods-Saxon form of the nuclear potential with parameters given by Akyüz and Winther [22], namely,

$$V_N(r) = \frac{-V_0}{1+\exp(\frac{r-R_0}{a})}. \quad (10)$$

The potential depth V_0 is expressed as

$$V_0 = 16\pi\gamma R_{12} a + \Delta V \quad (11)$$

in terms of the average surface tension coefficient

$$\gamma = 0.95\left[1 - 0.8\left(\frac{N_1 - Z_1}{A_1}\right)\left(\frac{N_2 - Z_2}{A_2}\right)\right] \text{ MeV fm}^{-2}, \quad (12)$$

the reduced radius

$$R_{12} = \frac{R_1 R_2}{R_1 + R_2}, \quad (13)$$

and the diffuseness parameter

$$a^{-1} = 1.17[1 + 0.53(A_1^{-1/3} + A_2^{-1/3})] \text{ fm}^{-1}. \quad (14)$$

In Eq. (10), the central radius $R_0 = R_1 + R_2$, where

$$R_i = (1.20A_i^{1/3} - 0.09) \text{ fm} \qquad (i = 1, 2). \quad (15)$$

Adjustments in the depth of the nuclear potential were introduced through the offset parameter ΔV, as discussed in the following sections.

The ℓ dependence of the barrier radius R_b and curvature $\hbar\omega$ was investigated with parameters pertaining to the one-dimensional BPM calculations described below. In ^{16}O + ^{148}Sm, R_b was found to vary by less than 5% in the (0–50)$\hbar$ range and $\hbar\omega$ can be represented as $\hbar\omega_\ell = \hbar\omega_0 + 6.1 \times 10^{-4}\ell^2$. In ^{64}Ni + ^{100}Mo, the variation in R_b is less than 3% in the (0–70)$\hbar$ range and $\hbar\omega_\ell = \hbar\omega_0 + 1.2 \times 10^{-5}\ell^2$. In the calculations for ^{16}O + ^{148}Sm we followed a full numerical treatment of Eqs. (1)–(5), whereas in ^{64}Ni + ^{100}Mo we resorted to the Wong approximation.

A. ^{16}O + ^{148}Sm reaction

The description of the ^{16}O + ^{148}Sm fusion excitation function was based on parameters extracted from the excitation function of ^{16}O + ^{144}Sm. In the latter system, the particular nature of the doubly magic ^{16}O and neutron magic ^{144}Sm imply a reduced subbarrier fusion enhancement. Data on ^{16}O + ^{144}Sm from Ref. [19] together with the (mass-scaled) measurement of Ref. [20] were described with the one-dimensional BPM. An offset of ΔV = 30.0 MeV in the nuclear potential depth was applied for this purpose. This adjustment was imposed in the ^{16}O + ^{148}Sm calculations.

The symbols in Fig. 1 show the measured fusion cross sections [19,20] for ^{16}O + ^{148}Sm as a function of the center of mass energy. Here, the fusion cross section is identified with the sum of the measured evaporation residue cross sections. The one-dimensional BPM (dashed curve) describes the data above 62 MeV, but underestimates the lower energy points. The extracted s-wave barrier parameters are listed in Table I. Based on these parameters, we determined the values of V_1, E_1, V_2, and E_2 required to fit the excitation function data in the EDBPM. A four-parameter least-squares procedure yielded the values given in Table I. The resulting excitation function is shown by the solid curve in Fig. 1. It provides a good description of the data in the whole energy range.

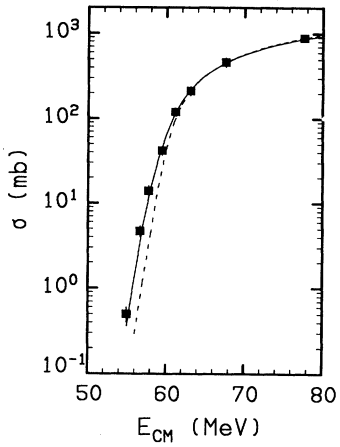

FIG. 1. Fusion cross sections in ^{16}O + ^{148}Sm reactions. The dashed and solid curves show the calculations with the one-dimensional and the energy-dependent barrier penetration models, respectively.

B. ^{64}Ni + ^{100}Mo reaction

The measured fusion excitation function in ^{64}Ni + ^{100}Mo reactions is shown on the top panel of Fig. 2. Data points below $E_{\text{c.m.}}$ = 141.7 MeV represent the sum of the evaporation residue cross sections including corrections for the unobserved channels [18]. The highest energy point includes only the sum of the evaporation residue cross sections obtained in a separate experiment [20]. The data are plotted at the center of mass energies corresponding to the effective beam energies where the reaction took place. The horizontal bars indicate the spread in the beam energies within the target for each measurement. They are consistent with the beam energy loss through the target [17,20]. The middle and bottom panels of Fig. 2 show the mean and mean-square angular momenta versus the center of mass energy. Data points below $E_{\text{c.m.}}$ = 141.7 MeV were obtained with a transformation of the evaporation residue γ multiplicity to the compound nucleus spin distributions [17]. At the highest bombarding energy the data points represent an estimate of the moments of the σ_ℓ distribution. These estimates were obtained from statistical model calculations that de-

TABLE I. Parameters employed in the one-dimensional BPM, EDBPM, and CCFUS calculations.

System	V_b (MeV)	R_b (fm)	$\hbar\omega$ (MeV)	V_1 (MeV)	E_1 (MeV)	V_2 (MeV)	E_2 (MeV)
^{16}O + ^{148}Sm	59.72	11.24	4.484	58.59	56.78	64.25	72.76
^{64}Ni + ^{100}Mo	137.61	11.45	3.499	127.82	125.19	141.97	143.15
^{64}Ni + ^{100}Mo (CCFUS)	138.64	11.34	3.407				

scribe closely the evaporation residue cross sections and γ-ray-fold distributions observed at this energy [20].

The one-dimensional BPM was applied with a nuclear potential strength adjusted by $\Delta V = -5.0$ MeV in order to reproduce the measured cross section at the highest energy. The predictions of the model for $\sigma_{\rm fus}$, $\langle \ell \rangle$, and $\langle \ell^2 \rangle$ are shown in Fig. 2 by the dashed curves. The experimental cross sections are comparable to the model predictions at the highest energies, but they are strongly underestimated as the bombarding energy decreases. The $\langle \ell \rangle$ and $\langle \ell^2 \rangle$ values are underestimated in the whole energy range, especially for $E_{\rm c.m.} < 137$ MeV, where the model predicts the existence of a plateau.

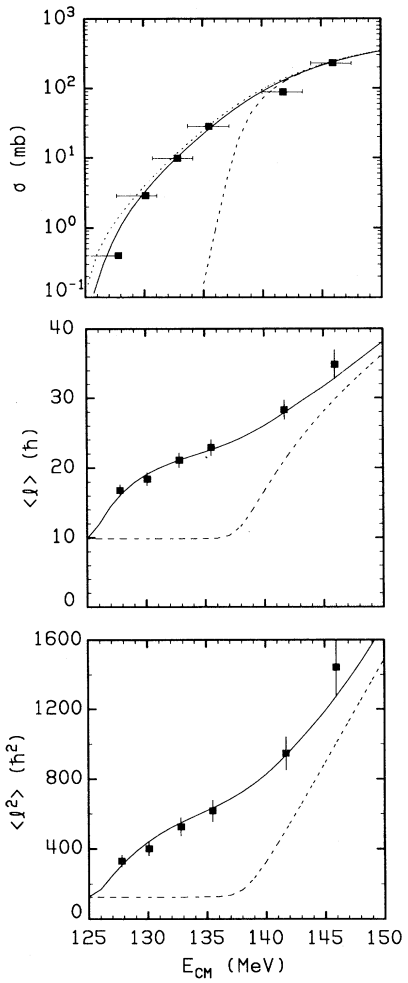

FIG. 2. Fusion cross sections and mean and mean-square angular momentum versus $E_{\rm c.m.}$ in ^{64}Ni + ^{100}Mo reactions. The data (symbols) are compared with calculations using the energy-dependent barrier penetration model (dotted and solid curves). The effect of target thickness is included in the calculations shown by the solid curves. The predictions of the one-dimensional barrier penetration model are given by the dashed curves.

We note that the available cross section data at the highest energies are not sufficient to establish the fusion barrier to a degree comparable to the reaction ^{16}O + ^{148}Sm. Therefore, in applying the EDBPM we follow an approach different than the one for the ^{16}O + ^{148}Sm reaction. Instead of utilizing the excitation function data, we extract an energy dependence of the fusion barriers from the experimental spin distributions. Using Eqs. (3), (5), and (6) and solving for V_b we obtain

$$V_b = \frac{\hbar\omega}{2\pi} \ln\left(\frac{\pi\lambda^2(2\ell+1)}{\sigma_\ell} - 1\right) + E - \frac{\ell(\ell+1)\hbar^2}{2\mu R_b^2}. \quad (16)$$

Representative values of the experimental partial wave cross sections around the average were used (see Fig. 4 of Ref. [17]). This angular momentum range is expected to involve minimal uncertainties due to unfolding procedures from γ-ray fold to γ multiplicity (M_γ) and the transformation from M_γ to ℓ. The one-dimensional BPM values of R_b and $\hbar\omega$ (Table I) including their weak ℓ dependence were used in order to extract V_b through Eq. (16). The extracted barriers are plotted in Fig. 3

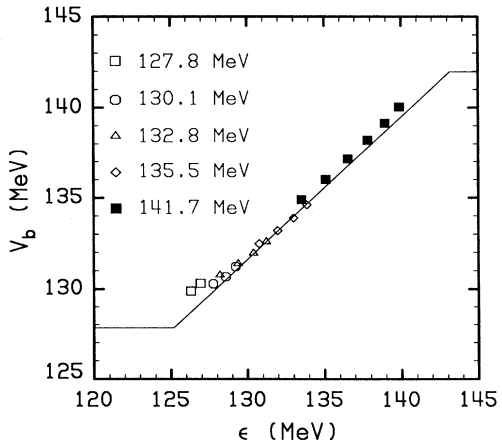

FIG. 3. Dependence of the extracted fusion barriers V_b (symbols) on the radial kinetic energy ϵ at the fusion barrier. Each symbol type corresponds to the indicated center of mass energy. The line segments show the parametrization employed in the calculations.

as a function of the radial kinetic energy at the barrier: $\epsilon = E_{\rm c.m.} - E_R$, where $E_R = \ell(\ell+1)\hbar^2/2\mu R_b^2$. Each symbol type corresponds to the indicated center of mass energy. At each energy, the barriers decrease with increasing E_R, i.e., with decreasing ϵ. An energy dependence consistent with the experimental trend of $V_b = V_b(\epsilon)$ was introduced in the EDBPM. The employed parameters in Eq. (9) are given in Table I and produce the dependence shown by the line segments in Fig. 3. The chosen value of V_2 is slightly larger than the one reported in the systematic study of Ref. [9]. We also used a value of V_1 smaller than the prediction of systematics, since there is no clear evidence for a saturation of the experimental V_b at low ϵ (see Fig. 3).

The calculated excitation function is shown by the dotted curve on the top panel of Fig. 2. It is consistent with the measurement at the highest energy, but overestimates the lower energy points. We point out that each cross section measurement represents the average yield in an interval $[E_{\rm c.m.}, E_{\rm c.m.} - \Delta E]$. Therefore, the predictions of the fusion models have to be energy averaged for the energy loss through the target in order to be compared with the data. Since the relevant energies for the target thickness correction are in the laboratory system, we energy-averaged the calculated excitation function in the laboratory system, using $\Delta E_{\rm lab} = 5.6$ MeV [17], and then transformed it to the center of mass. This produces the solid curve of Fig. 2. We note that including the effect of target thickness in the calculation affects the slope as well as the magnitude of the calculated excitation function, especially at low energies. This leads to an improvement in the overall description of the cross sections.

The effect of target thickness in the calculated centroids and average square of the σ_ℓ distributions was found to be less important than in the fusion cross sections. The calculated $\langle\ell\rangle$ and $\langle\ell^2\rangle$ are shown by the solid lines in Fig. 2. They provide a very good description of the data with the exception of the highest energy measurement which is slightly underestimated. Compared to the predictions of the one-dimensional BPM, we have a substantial improvement that reproduces the majority of the data. It must be stressed here that the good quality of the fits in Fig. 2 is not surprising, since the σ_ℓ values were used to restrict the choice of V_b. However, what is more important is that a single functional form of $V_b(\epsilon)$ [Eq. (9)] is consistent with the data for all bombarding energies.

C. Effect of channel coupling in ^{64}Ni + ^{100}Mo

Calculations for ^{64}Ni + ^{100}Mo were also performed with the simplified coupled-channels code CCFUS [23,24]. CCFUS treats the projectile and target inelastic excitation and transfer channels as independent modes that couple to the initial ground state. The resulting multidimensional barrier penetration problem is solved with a matrix diagonalization method. The variation of the coupling interaction in the barrier region is taken into account using a second-order expansion [23].

Our calculations with CCFUS were based on the nuclear potential given by Eqs. (10)–(15), with $\Delta V = -12$ MeV. The uncoupled calculation is shown again by the dashed lines in Fig. 4 where it is compared with the experimental $\sigma_{\rm fus}$, $\langle\ell\rangle$ and $\langle\ell^2\rangle$ versus $E_{\rm c.m.}$. The quality of agreement with the data is similar to the one-dimensional barrier penetration calculation of Fig. 2.

Initially, we considered the effect of coupling of the lowest (2^+ and 3^-) inelastic excitations in the projectile and target. Deformation parameters for the λ-pole excitations were employed from the tabulations of Refs. [25,26]. They are listed in Table II together with the corresponding coupling strengths [4]. Such a calculation was found to improve the description of the data, but it still underestimates both the low energy $\sigma_{\rm fus}$ and $\langle\ell\rangle$. This is in agreement with the results of Ref. [16]. In order

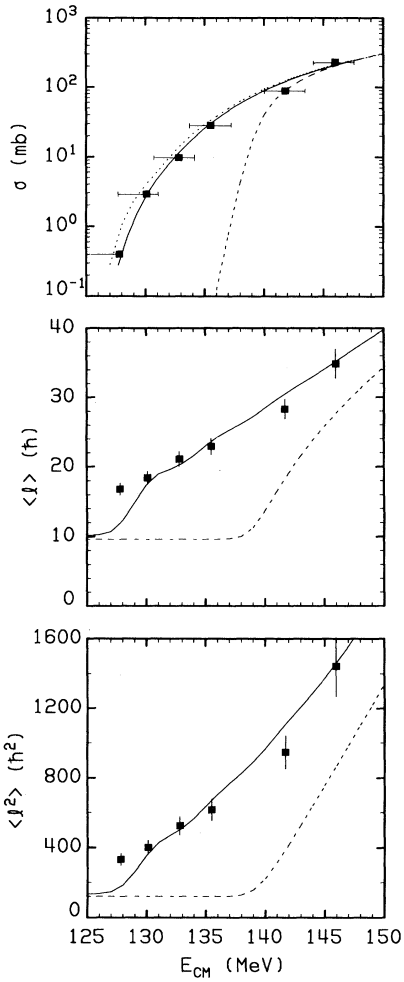

FIG. 4. Fusion cross sections and mean and mean-square angular momentum versus $E_{\rm c.m.}$ in ^{64}Ni + ^{100}Mo reactions. The data are compared with calculations involving the coupling to the lowest 2^+ and 3^- states of the projectile and target and additional coupling strengths (dotted and solid curves). The effect of target thickness is included in the calculations shown by the solid curves. The no-coupling limit is shown by the dashed curves.

TABLE II. Excitation energies E^*, deformation parameters β_λ, and coupling strengths F for the low-lying inelastic channels in ^{64}Ni + ^{100}Mo.

Nucleus	J^π	E^* (MeV)	β_λ	F (MeV)
^{64}Ni	2^+	1.35	0.18	−2.36
	3^-	3.56	0.23	−3.74
^{100}Mo	2^+	0.54	0.23	−3.35
	3^-	1.91	0.17	−3.12

to account for missing coupling strengths we introduced two couplings of strength $F = 2.6$ MeV at $\tilde{Q} = -1.5$ and -10.0 MeV in addition to the 2^+ and 3^- inelastic modes. Furthermore, we consider the effect of positive $\tilde{Q}$-value nucleon transfer channels as an enhancement mechanism. Table III gives the calculated effective $\tilde{Q}$ value for one- and two-nucleon transfers in ^{64}Ni + ^{100}Mo reactions.The effective $\tilde{Q}$ value is defined as $Q + \Delta E_C$, where Q is the ground state Q value and ΔE_C is the entrance channel Coulomb barrier minus that of the exit channel [4]. The $\tilde{Q}$ value for two-neutron pickup is positive. Therefore, this process is expected to enhance the subbarrier fusion rate. A coupling of strength $F = 3.8$ MeV at $\tilde{Q} = 0.97$ MeV was introduced for this purpose.

With the above couplings, the calculated fusion cross section versus $E_{\rm c.m.}$ is shown as the dotted curve in the top panel of Fig. 4. The calculation provides a reasonable description of the data, except for the lowest energy where it overestimates somewhat the lowest energy data points. Including the effect of target thickness, by averaging this excitation function within $\Delta E_{\rm lab} = 5.6$ MeV, gives the solid curve. This provides a good description of the fusion excitation function. The corresponding calculations for $\langle \ell \rangle$ and $\langle \ell^2 \rangle$ are shown as the solid curves in the middle and bottom panels of Fig. 4. Apart from an underprediction of the lowest and a small overprediction of the measurement at 141.7 MeV, the bombarding energy dependence of the data is well reproduced.

Concerning the magnitude and relative importance of the employed coupling strengths, we refer the reader to the remarks in Ref. [4] on the uncertainties of the form factors. The coupling strength for two-neutron pickup is comparable in magnitude to the one employed in the description of the ^{58}Ni + ^{64}Ni subbarrier fusion cross sections [27]. We note, however, the small yield of products associated with neutron transfer cited in Ref. [17]. Using a shallower nuclear potential would require weaker strengths for the description of low energy cross section measurements. However, confidence for such adjustments requires knowledge of experimental fusion cross sections at higher energies.

TABLE III. Effective $\tilde{Q}$ value for one- and two-nucleon transfer processes in^{64}Ni + ^{100}Mo reactions.

Process	$\tilde{Q}$ (MeV)
$1n$ stripping	−4.32
$1n$ pickup	−2.13
$1p$ stripping	−3.47
$1p$ pickup	−5.12
$2n$ stripping	−3.11
$2n$ pickup	0.97
$2p$ stripping	−1.77
$2p$ pickup	−5.72

One may recall the trends of previous analyses of the ^{64}Ni + ^{100}Mo reaction using the CCFUS code. DiGregorio and Stokstad [16] report that as a systematic trend, whenever the theory underestimates $\sigma_{\rm fus}$, it also underestimates $\langle \ell \rangle$. This is consistent with the calculations of Halbert *et al.* [17] employing standard parameters for the coupling strengths. However, Halbert *et al.* also showed that even if the fusion excitation function is reproduced, by using enhanced couplings, the $\langle \ell \rangle$ and $\langle \ell^2 \rangle$ are still underestimated at low energies. Vandenbosch [2] has been able to reproduce the shape of the fusion excitation function without an enhancement in the coupling strengths. This was made possible by a parameter adjustment that overestimated the cross section measurement at 141.7 MeV. However, the experimental $\langle \ell \rangle$ was still underestimated below $E_{\rm c.m.} = 132.8$ MeV.

In our analysis, the improvement in the simultaneous description of $\sigma_{\rm fus}$ and $\langle \ell \rangle$ is mainly due to taking into account the effect of target thickness in comparing the calculated $\sigma_{\rm fus}$ with the data. The target thickness correction in the calculated $\langle \ell \rangle$ versus $E_{\rm c.m.}$ is small. Therefore, using a theoretical excitation function that overestimates the experimental one at low energies results in a good description of the data after the energy averaging. This leads to an improved reproduction of the moments of the σ_ℓ distribution.

Fröbrich and Richert [12] have reported a consistent description of the ^{64}Ni + ^{100}Mo fusion cross section and $\langle \ell \rangle$ using a transport model by solving Langevin equations based on a surface friction model. Including a proper correction for the target thickness is expected to further improve the description of the data through the procedure of Ref. [12].

D. Angular momentum distributions

The ^{64}Ni-induced reactions have a significantly smaller mass asymmetry and show a substantially stronger subbarrier fusion enhancement than the ^{16}O-induced reactions. Therefore, we expect strong differences in the populated σ_ℓ distributions, when ^{164}Yb* is produced at the same excitation energy by the two reactions. The energy dependence of the σ_ℓ distributions is also of interest.

A comparison of the two reactions can be made through their reduced angular momentum distributions $\sigma_\ell / \pi \lambda^2$ [28]. We consider two typical excitation energies $E^* = 45$ and 53 MeV in ^{164}Yb*, which are below and near the Coulomb barrier for the ^{64}Ni reactions, and above the barrier for the ^{16}O reactions, respectively. In Figs. 5(a) and 5(b), we compare the reduced σ_ℓ distributions calculated with the previous models at bombarding energies matching these compound nucleus excitation energies. The dotted curves in Figs. 5(a) and 5(b) correspond to ^{16}O + ^{148}Sm and the solid ones to ^{64}Ni + ^{100}Mo, for the two bombarding energies, respectively, calculated

with the EDBPM. For each reaction, the corresponding ratios of the center of mass to the Coulomb barrier energies are also given in Fig. 5. For low-ℓ waves the reduced σ_ℓ distributions for ^{16}O + ^{148}Sm exhaust the unitarity limit shown by the dashed straight lines. For ^{64}Ni + ^{100}Mo, the respective distributions are much broader. According to the EDBPM, the unitarity limit is reached at the highest E^*. The distributions calculated with CCFUS for ^{64}Ni + ^{100}Mo are shown in Fig. 5 as the dashed curves. The distribution at the low energy, Fig. 5(a), is similar to the one calculated with the EDBPM, but some differences are apparent. At high energy, the two distributions are similar only in the high-ℓ region. The CCFUS distribution again shows a significant suppression of the low partial waves. This is a consequence of the higher barrier in the CCFUS calculation (Table I).

A common characteristic of both models for ^{64}Ni + ^{100}Mo is the presence of a large excess of high-ℓ partial waves compared to the ^{16}O-induced reaction. Furthermore, both models predict a suppression below the unitarity limit of the low-ℓ partial waves for the ^{64}Ni-induced reaction at low excitation energies.

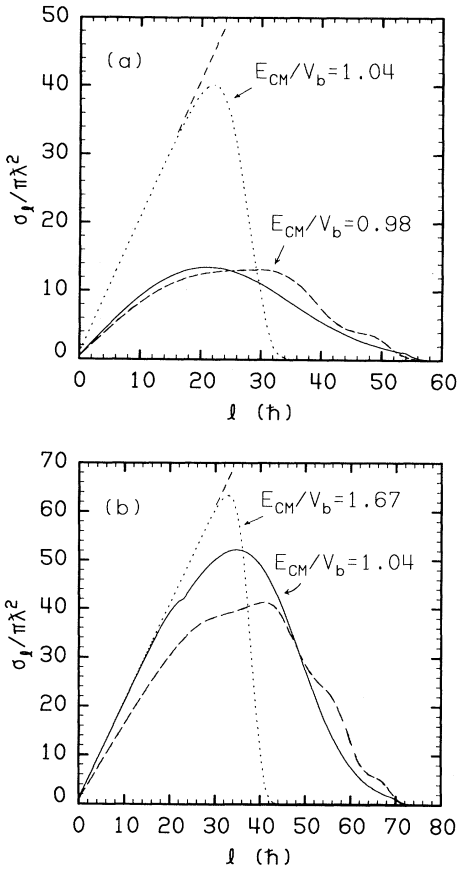

FIG. 5. Reduced angular momentum distributions in ^{16}O + ^{148}Sm (dotted curves) and ^{64}Ni + ^{100}Mo (solid curves) calculated with the energy-dependent barrier penetration model at bombarding energies matching the ^{164}Yb* excitation at (a) 45.0 and (b) 53.0 MeV. The dashed curves show the distributions calculated with CCFUS for ^{64}Ni + ^{100}Mo. The unitarity limit is shown by the dashed straight lines.

III. DECAY PROCESS

The differences in the populated compound nucleus states are expected to affect the measured evaporation residue yields in each reaction. In turn, these residue yields provide useful information about the populated spin distributions themselves. In order to demonstrate these effects we compare the yields in the two reactions, by using the decay fractions given by the ratio of a partial to the total evaporation residue cross section, for each exit channel (cf. Refs. [28,29]). A convenient representation for such a comparison involves the decay fractions as a function of the compound nucleus excitation energy. We present such a plot in Fig. 6 for the xn channels, where the open symbols refer to the ^{16}O + ^{148}Sm and the solid ones to the ^{64}Ni + ^{100}Mo reaction. Squares, circles, and triangles correspond to the $2n$, $3n$, and $4n$ channels, respectively. In the ^{16}O-induced reaction, the $2n$ decay fraction decreases monotonically with increasing excitation energy E^*. The 3n fraction increases initially with E^*, attains a maximum at 38 MeV, and then decreases. The $4n$ fraction shows a monotonic increase with E^*. In the ^{64}Ni-induced reaction, the trend of the corresponding decay fractions with E^* is essentially the same. However, there are striking differences when compared with the fractions of the ^{16}O-induced reaction. We observe a significant enhancement of the $2n$ fraction and a suppression of the the $4n$ fraction over the whole excitation energy range. The $3n$ fraction shows a suppression below 48 MeV, where it peaks, and an enhancement above it.

Because of the fact that both data sets are plotted with the compound nucleus excitation energy as a common abscissa, we expect the observed differences to arise from

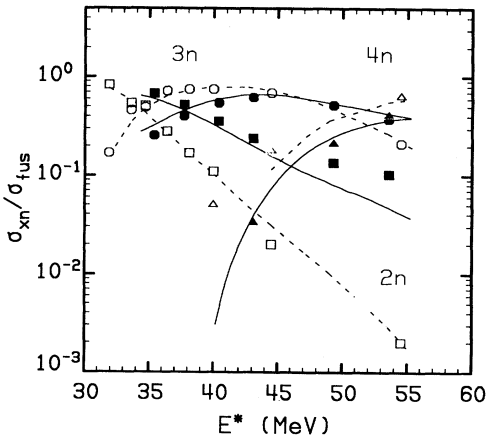

FIG. 6. Decay fractions of ^{164}Yb* formed in the fusion of ^{16}O + ^{148}Sm (open symbols) and ^{64}Ni + ^{100}Mo (solid symbols) as a function of the compound nucleus excitation energy. Evaporation residue channels involving emission of two, three, and four neutrons are indicated with squares, circles, and triangles, respectively. The dashed and solid curves show the results of statistical model calculations for the ^{16}O- and ^{64}Ni-induced reactions, respectively.

the populated compound nucleus spins in each reaction. Decays ending up in the $2n$ and $4n$ evaporation residues originate from high and low spins, respectively. In the ^{64}Ni-induced reaction, the enhancement of the $2n$ decay fraction can be associated with the excess of high-ℓ partial waves and the suppression of the $4n$ fraction with the low-ℓ properties of the σ_ℓ distributions. Statistical model calculations were performed in order to investigate this effect quantitatively.

The calculations were carried out with the code EVAP [30]. The level density formalism of Gilbert and Cameron [31] was employed with a level density parameter of $a = A/8.5$ MeV^{-1}. Penetrabilities for particle emission were calculated from the optical model using the global parametrizations of Wilmore and Hodgson [32], Perey [33], and McFadden and Satchler [34] for neutron, proton, and alpha particles, respectively. In the description of γ competition, emission of $E1$, statistical and collective $E2$, $M1$, and $M2$ γ rays were included. The $E1$ γ-ray emission strength function included the giant dipole resonance (GDR) with shape and position taken from systematics [35,36] and strength determined by the classical energy weighted sum rule [36]. The admixture of exchange forces in the nuclear force was assumed to be 50%. The GDR splitting due to deformation was included using a double Lorentzian GDR shape corresponding to an input prolate deformation parameter $\beta_{\rm GDR}$=0.2. The γ strengths for $M1$, statistical $E2$, $E2_{\rm coll}$, and $M2$ were set equal to 0.01, 10.0, 100.0, and 1.2 W.u., respectively.

The evaporation calculations made use of the σ_ℓ distributions produced by the fusion models described in the previous section. Because of the effect of target thickness in the ^{64}Ni + ^{100}Mo reaction, calculations were performed in 1 MeV steps in the bombarding energy range of the present study. The calculated residue excitation functions were energy averaged in a 5 MeV interval and the excitation functions corresponding to the measured cross sections were taken into account in the comparison of the decay fractions.

The results of the evaporation calculation with σ_ℓ distributions from the EDBPM are shown in Fig. 6 with dashed lines for ^{16}O + ^{148}Sm and solid lines for ^{64}Ni + ^{100}Mo. For ^{16}O + ^{148}Sm, the experimental $2n$ and $3n$ fractions are well reproduced by the calculation in the whole excitation energy range. The $4n$ fraction is underestimated at low E^*, but the agreement with the data improves with increasing E^*. In general, we have a good agreement between theory and experiment for this reaction. For ^{64}Ni + ^{100}Mo, the $3n$ and $4n$ decay fractions are reasonably well reproduced. The only significant discrepancy occurs in the $2n$ fraction which is underpredicted above $E^* \approx 45$ MeV. This is related with the tendency of the EDBPM calculation to underestimate $\langle \ell \rangle$ and $\langle \ell^2 \rangle$ at the highest energy.

The calculated decay fractions using σ_ℓ distributions from CCFUS are shown with the solid curves in Fig. 7. In the medium energy region, $40 < E^* < 50$ MeV, all three ratios are reasonably well reproduced. At the lowest energies, $E^* < 40$ MeV, the degree of agreement with the data deteriorates. This is related to the underprediction of $\langle \ell \rangle$ and $\langle \ell^2 \rangle$ in the corresponding $E_{\rm c.m.}$ range

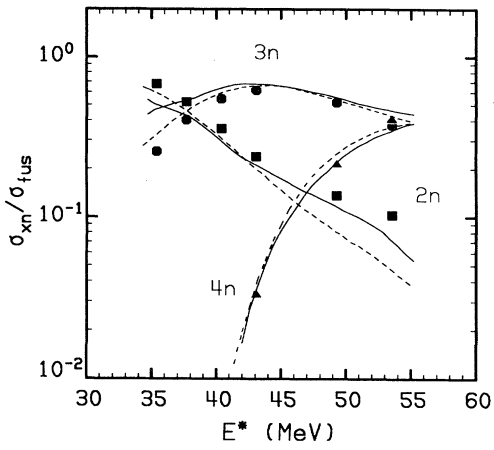

FIG. 7. Same as Fig. 6 for ^{64}Ni + ^{100}Mo only. The solid curves show the results of statistical model calculations based on σ_ℓ distributions from CCFUS. For comparison, the calculated fractions with the EDBPM are duplicated from Fig. 6 (dashed lines).

(Fig. 4). Above $E^* = 53$ MeV, the change in the slope of the calculated $2n$ decay fraction versus E^* is related to the onset of fission competition. For comparison, the calculation using the EDBPM σ_ℓ distributions is shown again in Fig. 7 with dashed lines. It is realized that the decay fractions tend to be reproduced by the statistical model whenever the fusion models tend to describe the moments of the spin distributions.

The previous calculations suggest that the behavior of the decay fractions in both reactions arises from the differences in the primary σ_ℓ distributions. The most prominent effect was observed in the exit channels involving the minimum and the maximum number of evaporated neutrons. These channels involve decays originating from the tails of the σ_ℓ distributions. Both reactions are expected to reach the unitarity limit at bombarding energies higher than the entrance channel Coulomb barrier. In this case, differences in the decay fractions are expected to appear only in the channels involving the minimum number of evaporated particles. Such an effect was demonstrated, some years ago, in reactions with a small entrance channel mass asymmetry by Alexander and Simonoff [29].

IV. SUMMARY AND DISCUSSION

In the present work, we presented an analysis of the formation and decay of the compound nucleus ^{164}Yb* in the reactions ^{16}O + ^{148}Sm and ^{64}Ni + ^{100}Mo. Fusion excitation functions and moments of the spin distribution in the second reaction were described well with a one-dimensional barrier penetration model with energy-dependent fusion barriers. The extraction of parameters in the EDBPM was greatly facilitated using the experimental σ_ℓ distributions.

Optical model analyses of elastic scattering cross sections close to the Coulomb barrier have given evidence for

energy-dependent interaction potentials. The energy dependence, known as the threshold anomaly, can be understood in terms of a dispersion relation [7]. It is believed to arise from the coupling of the elastic with nonelastic channels. Ramamurthy *et al.* [14] have suggested that an energy-dependent fusion barrier is also predicted from a macroscopic model of nuclear shape evolutions describing fusion. Here, the fusion barrier as a function of the radial kinetic energy varies between the value of the adiabatic (V_1) and the sudden barrier (V_2) in a linear fashion. Mohanty *et al.* [8] showed that the results of the CCFUS code can be reproduced by a simple barrier penetration calculation provided that the barrier heights are treated as a function of the radial kinetic energy at the top of the fusion barrier. It has also been shown that the difference ΔB between the sudden and the adiabatic barrier is an increasing function of the product Z_pZ_t of the atomic numbers of the colliding partners. The difference ΔB is responsible for the subbarrier fusion enhancement and includes all the processes associated with it. In the present analysis, a good reproduction of the data was obtained with $\Delta B = 5.7$ MeV for ^{16}O + ^{148}Sm and 14.20 MeV for ^{64}Ni + ^{100}Mo. These values are consistent with the systematic increase of ΔB with Z_pZ_t of Ref. [9].

Calculations with CCFUS were also able to reproduce the main features of the bombarding energy dependence of $\sigma_{\rm fus}$, $\langle \ell \rangle$ and $\langle \ell^2 \rangle$ for ^{64}Ni + ^{100}Mo. For this purpose, coupling strengths additional to those pertaining to the low-lying inelastic modes (2^+,3^-) in the projectile and target were introduced.

The fact that both models describe successfully most of the available ^{64}Ni + ^{100}Mo data was to be expected on the basis of the results of Ref. [8]. Some differences in the exact shape of the predicted σ_ℓ distributions originate mainly from the different parameters in the respective one-dimensional BPM calculations.

The statistical model with σ_ℓ distributions from the above fusion models has been able to reproduce most of the features of the compound nucleus decay formed in the two reactions. Some of the observed discrepancies might be able to be accounted for by the present models when additional experimental information becomes available.

ACKNOWLEDGMENTS

This work was supported by the Director, Office of Energy Research, Office of High Energy and Nuclear Physics, Nuclear Physics Division of the U.S. Department of Energy, under Contract No. DE-FG02-88-ER40406. We would like to thank Dr. R. J. Charity and Dr. L. G. Sobotka for fruitful discussions and Dr. M. L. Halbert for bringing to our attention Ref. [18].

[1] M. Beckerman, Rep. Prog. Phys. **51**, 1047 (1988).
[2] R. Vandenbosch, Annu. Rev. Nucl. Part. Sci. **42**, 447 (1992).
[3] C. H. Dasso, S. Landowne, and A. Winther, Nucl. Phys. **A405**, 381 (1983); **A407**, 221 (1983).
[4] R. A. Broglia, C. H. Dasso, S. Landowne, and G. Pollarolo, Phys. Lett. **133B**, 34 (1983).
[5] S. Landowne and S. C. Pieper, Phys. Rev. C **29**, 1352 (1984).
[6] S. Landowne and C. H. Dasso, Phys. Lett. **138B**, 32 (1984).
[7] G. R. Satchler, M. A. Nagarajan, J. S. Lilley, and I. J. Thompson, Ann. Phys. (N.Y.) **178**, 110 (1987).
[8] A. K. Mohanty, S. V. S. Sastry, and S. K. Kataria, Phys. Rev. Lett. **65**, 1096 (1990).
[9] A. K. Mohanty, S. V. S. Sastry, S. K. Kataria, and V. S. Ramamurthy, Phys. Rev. C **46**, 2012 (1992).
[10] T. Udagawa and T. Tamura, Phys. Rev. C **29**, 1922 (1984).
[11] P. H. Stelson, Phys. Lett. B **205**, 190 (1988).
[12] P. Fröbrich and J. Richert, Phys. Lett. B **237**, 328 (1990).
[13] C. E. Aguiar, L. F. Canto, and R. Donangelo, Phys. Rev. C **31**, 1969 (1985).
[14] V. S. Ramamurthy, A. K. Mohanty, S. K. Kataria, and G. Rangarajan, Phys. Rev. C **41**, 2702 (1990).
[15] W. J. Swiatecki, Phys. Scr. **24**, 113 (1981).
[16] D. E. DiGregorio and R. G. Stokstad, Phys. Rev. C **43**, 265 (1991).
[17] M. L. Halbert, J. R. Beene, D. C. Hensley, K. Honkanen, T. M. Semkow, V. Abenante, D. G. Sarantites, and Z. Li, Phys. Rev. C **40**, 2558 (1989).
[18] M. L. Halbert and J. R. Beene, in *Proceedings of the XIV Symposium on Nuclear Physics*, Cuernavaca, Mexico, 1991, edited by M. E. Brandan (World Scientific Publishers, Singapore, 1991).
[19] D. E. DiGregorio, M. diTada, D. Abriola, M. Elgue, A. Etchegoyen, J. O. Fernández Niello, A. M. J. Ferrero, S. Gil, A. O. Macchiavelli, A. J. Pacheco, J. E. Testoni, P. R. Silveira Gomes, V. R. Vanin, R. Liguori Neto, E. Crema, and R. G. Stokstad, Phys. Rev. C **39**, 516 (1989).
[20] J. L. Barreto, N. G. Nicolis, D. G. Sarantites, R. J. Charity, L. G. Sobotka, D. W. Stracener, D. C. Hensley, J. R. Beene, M. L. Halbert, C. Baktash, and M. Thoennessen, Phys. Rev. C **48**, 2881 (1993), preceding paper.
[21] C.Y. Wong, Phys. Rev. Lett. **31**, 766 (1973).
[22] Ö. Akyüz and A. Winther, in *Proceedings of the Enrico Fermi International School of Physics*, 1979, edited by R. A. Broglia, C. H. Dasso, and R. Ricci (North-Holland, Amsterdam, 1981), p. 492.
[23] C. H. Dasso and S. Landowne, Phys. Lett. B **183**, 141 (1987).
[24] C. H. Dasso and S. Landowne, Comput. Phys. Commun. **46**, 187 (1987).
[25] S. Raman, C. H. Malarkey, W. T. Milner, C. W. Nestor, Jr., and P. H. Stelson, At. Data Nucl. Data Tables **36**, 1 (1987).
[26] R. H. Spear, At. Data Nucl. Data Tables **42**, 55 (1989).
[27] R. A. Broglia, C. H. Dasso, and S. Landowne, Phys. Rev. C **32**, 1426 (1985).
[28] J. M. Alexander, H. Delagrange, M. Rajagopalan, M. F.

Rivet, and L. C. Vaz, Z. Phys. A **307**, 149 (1982).
[29] J. M. Alexander and G. N. Simonoff, Phys. Rev. **133**, B93 (1964).
[30] N. G. Nicolis, D. G. Sarantites, and J. R. Beene computer code EVAP (unpublished); evolved from the code PACE by A. Gavron, Phys. Rev. C **21**, 230 (1980).
[31] A. Gilbert and A. G. W. Cameron, Can. J. Phys. **43**, 1446 (1965).
[32] D. Wilmore and P. E. Hodgson, Nucl. Phys. **55**, 673 (1964).
[33] F. G. Perey, Phys. Rev. **131**, 745 (1963).
[34] L. McFadden and G. R. Satchler, Nucl. Phys. **84**, 177 (1966).
[35] A. Bohr and B. R. Mottelson, *Nuclear Structure* (Benjamin, New York, 1975), Vol. II.
[36] S. S. Hanna, in *Giant Multipole Resonances*, edited by F. Bertrand (Harwood, New York, 1980), Table I.